FISEVIER

Contents lists available at ScienceDirect

Journal of Power Sources Advances

journal homepage: www.sciencedirect.com/journal/journal-of-power-sources-advances





Influence of carbon content on the ionic and electronic conductivities of dense $Na_3V_2(PO_4)_3/C$ composites

Pradhyun Veerapanaicker Soundaraj ^a, Enkhtsetseg Dashjav ^a, Daniel Grüner ^b, Stephan Prünte ^a, Christian Dellen ^a, Frank Tietz ^a, ^{*}

- a Forschungszentrum Jülich GmbH, Institute of Energy and Climate Research, Materials Synthesis and Processing (IEK-1), 52425, Jülich, Germany
- b Forschungszentrum Jülich GmbH, Institute of Energy and Climate Research, Structure and Function of Materials (IEK-2), 52425, Jülich, Germany

ARTICLE INFO

Keywords:
Sodium vanadium triphosphate
Carbon
Ionic conductivity
Electronic conductivity
Composites

ABSTRACT

Sodium vanadium triphosphate (Na $_3$ V₂(PO₄) $_3$, NVP) is a promising cathode material for Na-ion batteries. Due to its intrinsically low electronic conductivity, it is usually mixed or coated with carbon. However, so far there have been no systematic studies on the ionic and electronic conductivity of carbon-coated NVP particles. In this work, NVP with varying carbon contents are prepared. The powders are sintered as single pellets or sandwiched between a solid electrolyte for measurements in an ion blocking and non-ion blocking configuration. In these two different configurations, two different electrodes are attached and several electrochemical characterization techniques are applied such as impedance spectroscopy, chronoamperometry, and four-point measurements. The NVP/C composites with carbon content >0.1 wt% show a high degree of densification and an amorphous carbon network. The conductivity of NVP in composites with carbon content <0.1 wt% shows dominating ionic conduction with an average value of ~2 × 10^{-6} S cm⁻¹. NVP/C samples with carbon contents >0.1 wt% show a dominance of electronic conduction in the range of 0.01–0.2 mS cm⁻¹ because of the percolated carbon network at the grain boundaries. The ionic conductivity, however, remains almost constant in the same order of magnitude (~6 × 10^{-6} S cm⁻¹).

1. Introduction

Na-ion batteries (NIB) have emerged as one of the best alternatives for Li-ion batteries due to the higher abundance of sodium in the Earth's crust [1] and, hence, the better availability of sodium products. In fact, the development of sodium batteries will help to reduce the dependence on critical raw materials, i.e. materials with a (geopolitical) significant supply risk [2] such as Co, Ni, Cu, and Li. So-called post-lithium technologies based on non-critical elements such as sodium, represent a long-term opportunity to avoid material dependence on oligopolistic suppliers of raw materials [3]. Therefore, research partially has shifted towards the development of cathode materials suitable for NIB and all-solid-state Na-batteries (ASSNB). One of the first examples of possible cathodes for NIB are the phosphates with an open framework structure [4]. Among them, Na₃V₂(PO₄)₃ (NVP) was tested in NIB in 2012 [5]. Since it crystallizes in the kosnarite structure [6], similar to the well-known highly ion-conductive solid electrolytes Na_{3+x}Zr₂₋ $Si_{2+x}P_{1-x}O_{12}$ (NZSP) with 0.3 < x < 0.5 [7], and with a stability up to 4.5 V νs . Na/Na $^+$ in ASSNB [8], it has received increasing attention even though vanadium is also a critical element. As the redox reaction of vanadium has been exploited in NIB typically in the voltage window of 0–4 V νs . Na/Na $^+$, V(III) oxidizes to V(IV) at 3.4 V νs . Na/Na $^+$ giving a specific capacity of 117.9 mAh g $^{-1}$ [1]. To our knowledge, the electronic conductivity of pure NVP has not yet been clearly determined. Data were only reported for Li₃V₂(PO₄)₃, which also crystallizes with the Na₃V₂(PO₄)₃ structure as 10 $^{-8}$ –10 $^{-10}$ S cm $^{-1}$ [9–11].

To overcome the intrinsically low electronic conductivity of NVP [12], several methods have been studied such as carbon coatings [13–17], substitution with other metal ions [18–21], and reducing the particle size [1]. Even though NVP/C is a well-known cathode material, we are aware of only one systematic study on the total conductivity of NVP/C composites. This very new publication deals with the cold sintering of mixtures composed of NVP with carbon black or carbon fibers [22]. The influence of the carbon content on the electrical properties of NVP/C and its efficacy in transmitting electrons and Na $^+$ ions are dependent on the processing and on the carbon source used. Some of the

E-mail address: f.tietz@fz-juelich.de (F. Tietz).

 $^{^{\}ast}$ Corresponding author.

studies that have reported ionic and electronic conductivities are listed in Table 1.

In this work, the impact of carbon on the transport properties of NVP/C composites is comprehensively investigated using samples with very high density to avoid the influence of porosity. Field-assisted sintering technique/spark plasma sintering (FAST/SPS) is used to sinter NVP/C composites with different carbon contents. The electronic conductivity and the ionic conductivity are examined using impedance spectroscopy on samples with ion-blocking and non-ion blocking configuration.

2. Experimental

2.1. Materials

For the synthesis of NVP/C composites, sodium dihydrogen phosphate (NaH₂PO₄, Sigma-Aldrich, ≥ 99 % purity), ammonium vanadate (NH₄VO₃, Merck Supelco, ≥ 99.0 % purity) and citric acid (C₆H₆O₇, Merck Supelco, ≥ 99.0 % purity) were stoichiometrically mixed in the ratio of 3: 2: x, respectively, where x represents varying molar fractions of citric acid (0, 0.5, 1, 1.25, 1.50, 1.75, 2, 3), to achieve the desired residual carbon amount in the system. The powders were added to a beaker containing 150 ml water and 30 ml ethanol, and were then stirred for 12 h at 100 °C until the mixture formed a gel. The gel was dried in a vacuum oven at 100 °C overnight. Then, the as-dried green powders were heat-treated in two steps. In the first step, the powders were heated to 300 °C at 60 K/h and held for 4 h in an Ar atmosphere to remove residual volatile hydrocarbons. In the second step, the powders were heat-treated at 800 °C at 60 K/h and held for 10 h in reducing atmosphere (Ar with 2 % H₂) to convert the organic residues to carbon

The synthesis of solid electrolyte NZSP is reported elsewhere [27]. Subsequently, heat-treated NVP/C and NZSP powders were milled separately at 500 rpm for 4 h using 10 mm zirconia balls (Pulverisette 7, Fritsch GmbH, Germany).

2.2. Powder characterization

The residual carbon amount was determined for every NVP/C powder by combusting a sample in oxidizing atmosphere and detecting the CO2 peaks in the infrared spectrum (RC612, LECO Corporation, USA). The formed phases of NVP/C and NZSP were investigated using X-ray diffraction (XRD) on a D4 Endeavor diffractometer (Bruker GmbH, Germany) in the 20 range from 10° to 80° in steps of 0.02° using Cu-K $_\alpha$ radiation and equipped with a Lynxeye detector (Bruker GmbH, Germany). The HighScore software (Malvern Panalytical Ltd., UK) with the PDF-2 database (ICDD) was used for phase identification.

2.3. FAST/SPS

The ball-milled powders were placed inside a pressing tool made of TZM alloy (titanium-zirconium-molybdenum) with an inner diameter of 12 mm (see Fig. 1a). The inner walls of the pressing mold were covered with a thin graphite layer and sintering was carried out using a HP-D5 device (FCT Systeme GmbH, Germany). The first report on SPS-sintered NVP samples records a sintering temperature of 900 $^{\circ}\text{C}$ at a

pressure of 50 MPa [28]. However, it has been reported elsewhere that NVP and NZSP decompose at temperatures above 800 °C, forming Na₄SiO₄ and SiP products [29]. Other groups sintered NVP samples at 600 °C with a pressure of 102 MPa [30]. Due to the low temperature and pressure, the density of the samples was as low as 80 % of the theoretical density. Building on the previous results, in this work, the NVP/C powders were heated to 800 °C at 6000 K/h at a pressure of 440 MPa and held for 10 min in Ar atmosphere before cooling to room temperature at 1500 K/h to prevent thermal-shock-assisted cracking. The profile of temperature, pressure, and sample density is schematically shown in Supplementary Fig. S1a. The parameters were optimized in several experiments at 675 °C, 750 °C, and 800 °C at a constant pressure of 440 MPa to synthesize dense NVP/C pellets without decomposition. Furthermore, after FAST/SPS, samples were polished using sandpaper (400, 800, 1200 grits) to remove the graphite layer. Two configurations of pellets were prepared (Fig. 1b), one with pristine NVP/C or NZSP as a single layer and the other with NVP/C sandwiched between NZSP sintered at the temperature and pressure mentioned above.

2.4. Characterization

The morphology of the ball-milled NVP/C powders and the polished surface of the sintered samples were examined using scanning electron microscopy (SEM, Merlin, Carl Zeiss Microscopy, Germany) coupled with energy-dispersive X-ray spectroscopy (EDX, X-Max Extreme and X-Max 80 detectors, Oxford Instruments, UK) for elemental analysis. EDX data were analyzed using the associated Aztec software. For high-resolution SEM studies, polished cross-sections of selected samples were prepared by Ar ion milling (SM09010 Cross Section Polisher, Jeol, Japan). Raman spectroscopy was performed on the pellet surfaces using a Renishaw inVia confocal Raman microscope equipped with a solid-state laser with a wavelength of 532 nm. In order to improve measurement statistics, a single area was mapped with at least 400 Raman spectra.

2.5. Conductivity measurements

Impedance spectroscopy, chronoamperometry and four-point DC measurements were performed to quantify the ionic and electronic conductivity of the sintered samples. For impedance spectroscopy a multichannel potentiostat (VMP300, Biologic, France) was used at a constant temperature of 25 °C equipped with a controlled climate chamber (VT4002, Vötsch, Germany). The single-layered pristine NVP/ C pellets were coated with Au blocking electrodes. When coated with Na metal (non-blocking) electrodes, the tri-layered pellets with NVP/C between NZSP should allow Na⁺ ions to pass through the tri-layer setup while filtering electron transportation at lower frequencies thereby helping to better resolve the ionic contribution of NVP/C. Similar configurations have been reported elsewhere for different materials [31]. In each sample configuration, either sputtered Au films or thin layers of sodium metal were used as electrodes. Impedance spectroscopy was performed with 10 mV voltage perturbation in the frequency range from 7 MHz to 100 mHz. The results were then interpreted using EC-lab and Z-view software and fitted with appropriate equivalent circuits. Chronoamperometry measurements were performed on NVP/C samples and

Table 1Conductivity values reported for NVP/C composites.

Sample	Processing method	Total conductivity at 25 $^{\circ}$ C (S cm ⁻¹)	Reference
NVP	Infiltration and sintering	$1 imes 10^{-6}$	[12]
NVP/C annealed at 600 °C	Tape casting	$2.1 imes 10^{-5}$	[23]
NVP/C annealed at 800 °C	Tape casting	$1.3 imes10^{-1}$	[24]
NVP/C with 5 wt% Na ₂ O-Nb ₂ O ₅ -P ₂ O ₅	Tape casting	$2.9 imes 10^{-5}$	[24]
NVP/C	Conventional sintering (Ar/5% H ₂)	6.18×10^{-6} (ionic)	[25]
NVP/C	Conventional sintering (Ar)	4.47×10^{-4} (electronic)	[26]

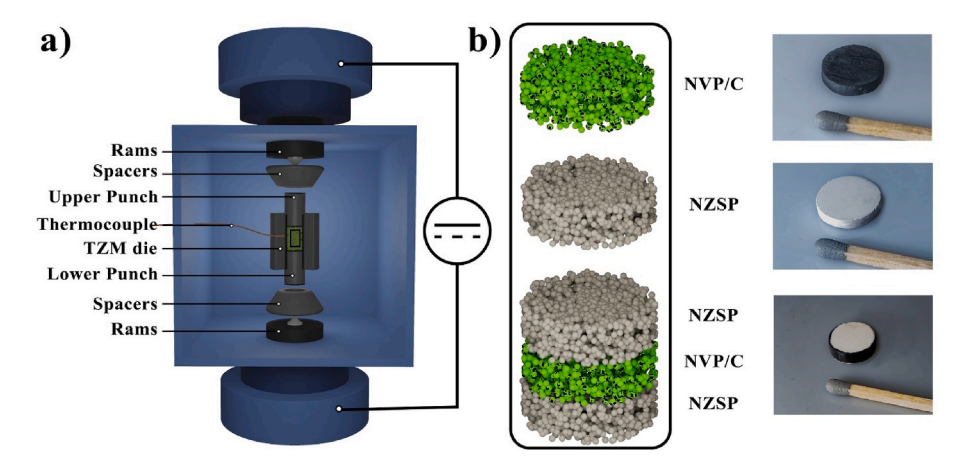


Fig. 1. a) Setup of pressing mold for FAST/SPS, b) different types of powder compacts as schematics and photographs of sintered samples.

tri-layer NVP/C samples by applying a constant voltage of 100 mV and measuring the current after 48 h. The four-point DC measurements were carried out using a van-der-Pauw apparatus [32] constructed in-house. Constant currents of 20 mA to -20 mA in a decrement of 5 steps were applied across the diameter of the samples and the voltage drop was measured from two other points over the diameter perpendicular to the plane of applied current probes using a multimeter (2400 source master, Keithley instruments, USA). The quality of the measured conductivities (σ) was assessed using a simplified error analysis, taking into account the dimensions of the test specimens and the measured electrical parameters:

$$\frac{\Delta\sigma}{\sigma} = \left|\frac{\Delta R}{R}\right| + \left|\frac{\Delta A}{A}\right| + \left|\frac{\Delta h}{h}\right|$$
 Eq. (1)

where R, h, and A are the resistance in ohm, the thickness in cm, and the area of the electrode in cm². For the impedance measurements, the chronoamperometry measurements and the four-point DC measurements, ΔR is the error of the fitted equivalent circuit parameters, the fluctuation of the measured current around the mean current value ($U_{\text{const.}}/\Delta I$), and the standard deviation of the linear regression of the measured U/I values, respectively. Similarly, ΔA and Δh are the uncertainties in the determination of the geometric values of the samples (in the case of the four-point DC measurements $\Delta A = 0$). The errors given in the following chapters are the $\Delta \sigma$ values determined with equation (1).

3. Results and discussion

3.1. Material characterization

The mass fraction of carbon and the density of the NVP/C sintered samples are listed in Table 2. Hereafter, the samples will be referred to as NVP/C_x.xx, where the x.xx represents the weight percentage of carbon shown in Table 2. For samples with low carbon content, i.e. NVP/C_0.03

Table 2Carbon content, density after FAST/SPS and the amount of citric acid used during synthesis.

Sample	Citric acid (mol)	Carbon (wt%)	Density (%)
NVP/C_0.03	0	0.03	95
NVP/C_0.04	0.5	0.04	96
NVP/C_0.42	1	0.42	98
NVP/C_0.83	1.25	0.83	99
NVP/C_2.67	1.5	2.67	99
NVP/C_3.32	1.75	3.32	99
NVP/C_5.80	2	5.80	99
NVP/C_10.9	3	10.9	99

and NVP/C_0.04, the density is relatively low. For all other samples with carbon weight percentages of 0.83 % and higher, the density is higher than 99 % theoretical density. The theoretical density of NVP and carbon is taken as 3.15 g cm $^{-3}$ and 2.25 g cm $^{-3}$ [33], respectively.

The XRD patterns of NVP/C_5.80 and NZSP powder heat-treated at 800 °C and 1250 °C, respectively, were analyzed with the Rietveld method using the structure model with symmetry (ICSD 248140 for NVP and ISCD 62386 for NZSP; see Fig. 2c and d). The refinement started with the subtraction of the background, refinement of lattice parameters and zero shifts using the Pawley fit, converging to an $\rm R_p$ value of 5.7 %. In a second step, Rietveld refinements were carried out with and without restriction for the occupational parameters of Na atoms. All other structural.

parameters such as atomic positions, site occupation factors, and temperature factors, were keptconstant, as shown in Table S1. The best goodness of fit for refinements was found with the Pawlev fitting with fixed atomic parameters of all atoms. This was then used for all NVP/C specimens. The refined NVP/C 5.80 is a single-phase material with hexagonal lattice parameters a = 8.7264(2) Å and c = 21.8493(9) Å with reliability factors (R $_p = 5.68 \ \%$ and wR $_p = 7.75 \ \%$). The XRD pattern of the analogue SPS-sintered NVP/C pellet (not shown here) showed no additional peaks. This, in turn, suggests that FAST/SPS parameters are optimum for densification without any decomposition of NVP. The refinement of the XRD pattern of NZSP was started using two models with rhombohedral and monoclinic symmetry, as given in the database (ICSD 62386 and ICSD 81695, respectively). Only profile fitting was applied keeping all structural parameters constant. According to the profile fitting, the best R-values were achieved with a mixture of both phases: 98 % rhombohedral phase with R3c symmetry (e. g. Na_{3,35}Zr₂₋ Si_{2.35}P_{0.65}O₁₂, ICSD 62386) and small amount of 2 % monoclinic phase with space group C2/c (corresponding to Na_{3,29}Zr_{1,94}Si₂PO₁₂, ICSD 81695; see Fig. 2d). The refined lattice parameters for the main phase are a = 9.0782(6) Å and c = 22.8332(10) Å ($R_p = 2.81$ %, $wR_p = 3.97$

3.2. Sintering behavior

During SPS, pulsed DC current is applied to the ceramic green body causing plasma discharge (electrons and ions) [34] between two particle surfaces, which in turn creates high temperatures at these local regions on the surface, causing neck formation between the two particles (Fig. S1c, left image). In the initial stages of sintering, at low temperature, the surface diffusion dominates as the sintering mechanism of NVP/C. The residual carbon on the NVP surface (Fig. S1b, left image) moves from the surface of the NVP particles (higher potential) to the neck regions (lower potential) formed between NVP particles [35], thus forming an initial grain boundary.

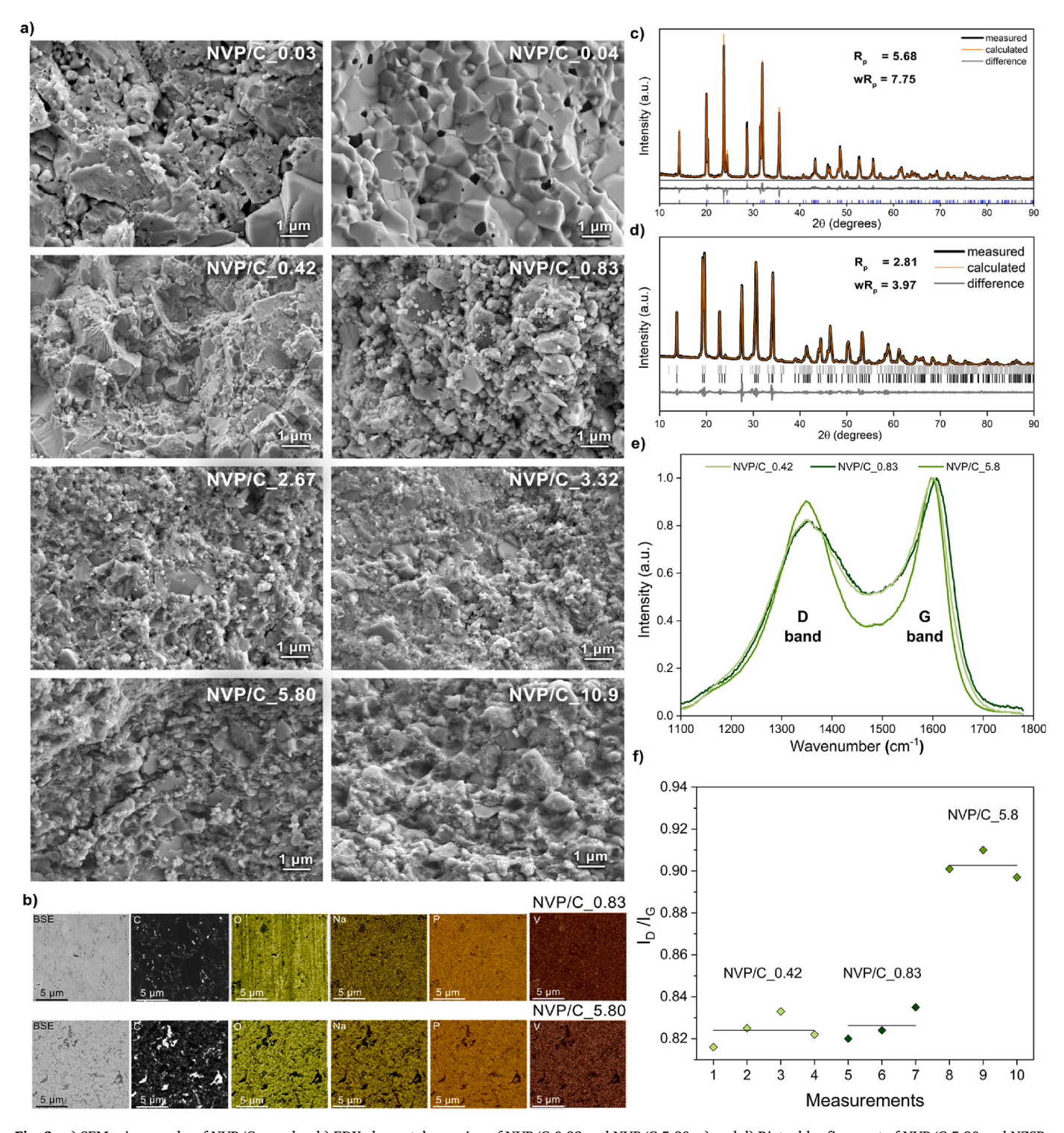


Fig. 2. a) SEM micrographs of NVP/C samples, b) EDX elemental mapping of NVP/C_0.83 and NVP/C_5.80, c) and d) Rietveld refinement of NVP/C_5.80 and NZSP, respectively, e) Raman spectra of amorphous carbon in NVP/C samples and f) determined I_D/I_G ratios. The horizontal lines are the corresponding mean values.

At higher temperatures, pores are formed between the NVP particles. During this stage of sintering, the pore size shrinks either by surface diffusion or by grain boundary diffusion or both (Fig. S1c, center image) [34]. At this stage the pores are all interconnected to form pore channels. Surface diffusion aids in transporting the carbon to the grain boundaries and thereby densifying the sample. It is obvious from Fig. 2a that NVP/C_0.03 and NVP/C_0.04 are at the intermediate stage of sintering with connected pores and some isolated pores.

Further densification occurs due to the volume and grain boundary

diffusion at maximum temperature (Fig. S1b, center and right image). The residual carbon diffuses at the grain boundaries (Fig. S1c, right image), causing further densification during the isothermal final stage of sintering (Fig. 2a). This corroborates the densification phenomenon with a higher percentage of carbon in the NVP/C composites, as shown in Table 1. The SEM images of fracture surface of NVP/C_0.44 to NVP/C_10.9 show densification of NVP with carbon at the grain boundaries. It is evident from Fig. 2b and c that carbon aggregates at the grain boundaries in NVP/C_0.83 and in NVP/C_5.8. Due to the increasing carbon content, carbon

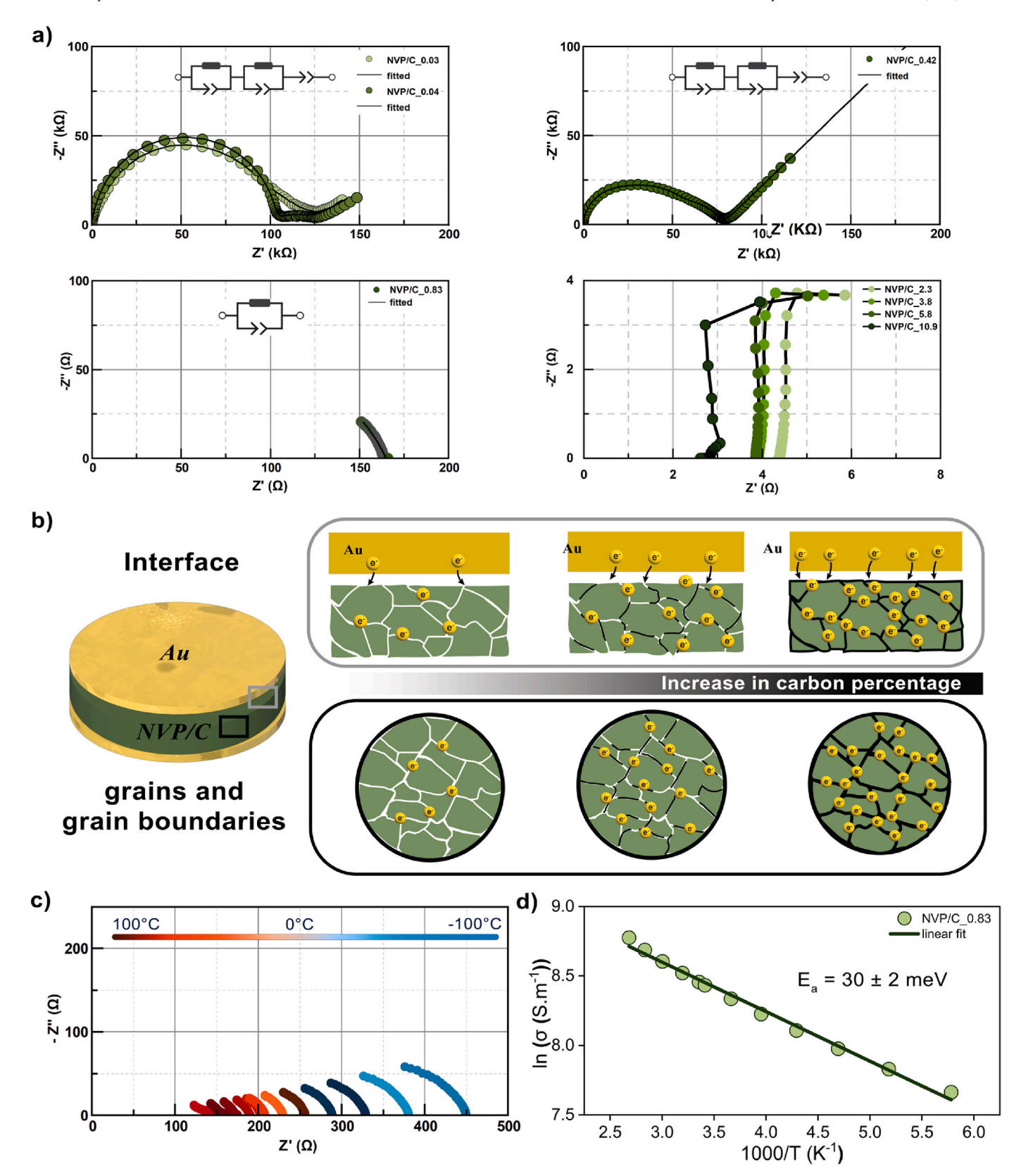


Fig. 3. a) Impedance spectra of each NVP/C sample, b) graphical representation of carbon content and increase in electronic conductivity, c) temperature-dependent impedance measurement of NVP/C_0.83, d) Arrhenius plot for calculation of activation energy of the dominant transport process.

can be seen both at the NVP grain boundaries as thin layers and between the NVP particles as lumps, mainly at triple points and other former voids.

3.3. Raman spectroscopy

Raman spectra and the intensity ratio of the D mode and G mode of NVP/C 0.42, NVP/C 0.83 and NVP/C 5.80 samples are shown in Fig. 2e and f. For amorphous carbon, the presence of diamond-like carbon (D mode, sp³ hybridization) at around 1350 cm⁻¹ can be attributed to the breathing mode of sixfold rings with A_{1g} symmetry. The presence of graphite-like carbon (G mode, sp² hybridization) at around 1590 cm⁻¹ corresponds to in-plane bond-stretching motion of pairs of carbon atoms with E_{2g} symmetry [36,37]. The absence of reflections that could be assigned to graphite in XRD patterns (Fig. 2c) further confirms the presence of amorphous carbon in all samples. Generally, the ratio of band intensities I_D/I_G is usually used to estimate the degree of graphitization of carbon [38]. In the case of amorphous carbon, however, the ratio of I_D/I_G is ascribed to the disordering degree of carbon. As the carbon content in the samples increases, the intensity of the D mode increases and as a result the I_D/I_G ratio increases (shown in Fig. 2f), indicating a tentatively higher content of hexagonal structure units. With regard to the electronic conductivity, it can be assumed at this point that a higher carbon content and a thicker coating of the NVP particles have a stronger influence than the change in the I_D/I_G ratio. A more detailed investigation of amorphous carbon would be necessary to determine this more clearly.

3.4. Conductivity measurements

3.4.1. Total conductivity of NVP/C composites

The impedance spectra of the NVP/C samples with ion-blocking electrodes are shown in Fig. 3. NVP/C_0.03 and NVP/C_0.04 samples show two semicircles. The total conductivity was determined from the fitted RC circuit of the first large semicircle at high frequencies and its right intercept with the abscissa where the imaginary part $Z'' \rightarrow 0$. This point corresponds to the ionic conductivity of the samples, since nearly no carbon is present. Here the values are $1.6 \pm 0.2 \times 10^{-6} \ \text{S cm}^{-1}$ and $2.5 \pm 0.3 \times 10^{-6}$ S cm⁻¹, respectively (Fig. 3a and Table 3). This is in accordance with previously reported ionic conductivities of pristine NVP [12]. The R_{ct} (charge transfer resistance) in parallel with C_{dl} (double layer capacitance) at medium frequencies, visible as a small second semicircle, corresponds either to the generally assumed resistance of charge transfer kinetics or to a geometrical/dynamic constriction created by inhomogeneities at the sample electrode interface [39]. As the ideal capacitance is uncommon in normal electrochemical systems, it has been replaced by a constant phase element (CPE) in the equivalent circuit. The R_{ct} values of NVP/C 0.03, NVP/C 0.04 and NVP/C_0.44 are 24.5 k Ω , 21.3 k Ω , and 15.2 k Ω , respectively. The charge transfer resistance decreases with increasing carbon content to a point where the interfacial or charge transfer resistance is no longer noticeable (NVP/C_0.83). A further increase in carbon results in ohmic resistive behavior composed of an inductance at high frequencies originating from the cables and pure resistance at low frequencies of the samples (NVP/C 2.3 to NVP/C 10.9).

Table 3Measured total conductivity of the NVP/C samples.

Total conductivity (S cm ⁻¹)		
$1.6 \pm 0.2 \times 10^{-6}$		
$2.5 \pm 0.3 \times 10^{-6}$		
$1.0 \pm 0.1 \times 10^{-5}$		
$9.9 \pm 0.9 \times 10^{-4}$		
$1.20\pm0.05\times10^{-1}$		
$1.63 \pm 0.07 \times 10^{-1}$		
$1.79\pm0.08 imes10^{-1}$		
$2.09\pm0.11 imes10^{-1}$		

To calculate the total conductivity for each sample, equation (2) is used:

$$\sigma = \frac{h}{R * A}$$
 Eq. (2)

where R, h, and A are the resistance, thickness, and area of the electrode as mentioned above.

The calculated total conductivities are listed in Table 3. The increase in conductivity of over six orders of magnitude is ascribed to the increasing carbon at the grain boundaries (Fig. 2b) present as amorphous carbon (Fig. 2e and f). The carbon helps to minimize the electronic resistance at grain boundaries as well as at the Au|NVP/C interface, thereby enabling fast electron transport through the sample as illustrated in Fig. 3b.

The sample NVP/C_0.83, in particular, shows an increased total conductivity of $1\times 10^{-3}~S~cm^{-1}$ with a semicircle response from the impedance at high frequencies, corresponding to the total resistance of the sample. At lower frequencies, the impedance touches the x-axis (Z'' = 0) and does not show a contribution of double-layer capacitance or Warburg impedance. This is characteristic of electronic conduction at low frequencies [31]. The temperature-dependent impedance measurements shown in Fig. 3c and the corresponding Arrhenius plot (Fig. 3d), result in a very low activation energy of 30 ± 2 meV, which can be ascribed to the predominant electronic conduction of the broken carbon network along grain boundaries (Fig. 3b). This interrupted carbon network still has small contributions of polarized ions and electrons and hence a small capacitive response.

The total conductivity of NVP samples with higher carbon contents comprises both ionic and electronic conductivities and behave as mixed electronic and ionic conducting (MEIC) materials. In order to decipher ionic and electronic contributions in the NVP/C composites, the experimental setup and equipment were configured to measure certain aspects of the samples.

3.4.2. Electronic conductivity of NVP/C composites

The electronic conductivity of the NVP/C samples is shown in Fig. 4a. Chronoamperometry was used to determine the electronic conductivity of NVP/C 0.03 and NVP/C 0.04 because of their low electronic conductivity (light green circles). For samples with higher carbon content, the electronic conductivity was measured using the four-point measurement setup [32], as shown in Fig. 4b. The four-point measurement setup allows the electronic conductivity of a material to be determined by eliminating the sample electrode interfacial resistance [40,41]. To the best of our knowledge, the electrical conductivity of NVP samples is reported to be low [1,42-46], but electronic conductivity values, however, have not yet been reported. The electronic conductivity was found to be in the order of 10^{-9} – 10^{-8} S cm $^{-1}$, with 5.0 \pm 1.1 $\times~10^{-9}~S~cm^{-1}$ and 6.7 $\pm~1.4~\times~10^{-9}~S~cm^{-1}$ for NVP/C_0.03 and NVP/C_0.04, respectively, which is in accordance with the previously reported values for $\text{Li}_3\text{V}_2(\text{PO}_4)_3$ [9–11]. NVP/C samples with C content >2 wt% revealed a plateau in electronic conductivity (Fig. 4a), indicating a percolating network of conductive amorphous carbon.

3.4.3. Ionic conductivity of NVP/C composites

Impedance spectra of NVP/C_0.03 and NVP/C_5.80 with different blocking electrodes and two different configurations are shown in Fig. 4c. Rather than choosing the starting point of the semicircle and assuming the ionic and electronic resistors are in parallel in the ion-blocking electrode setup and calculating the ionic conductivity of the sample [24], we propose that the total resistance of the configuration [electrode|NZSP|NVP/C|NZSP|electrode] corresponds to the ionic resistance of the NVP since NZSP would only allow the ions to pass through the NZSP|NVP/C interface [31], while its ionic conductivity is three orders of magnitude higher than NVP.

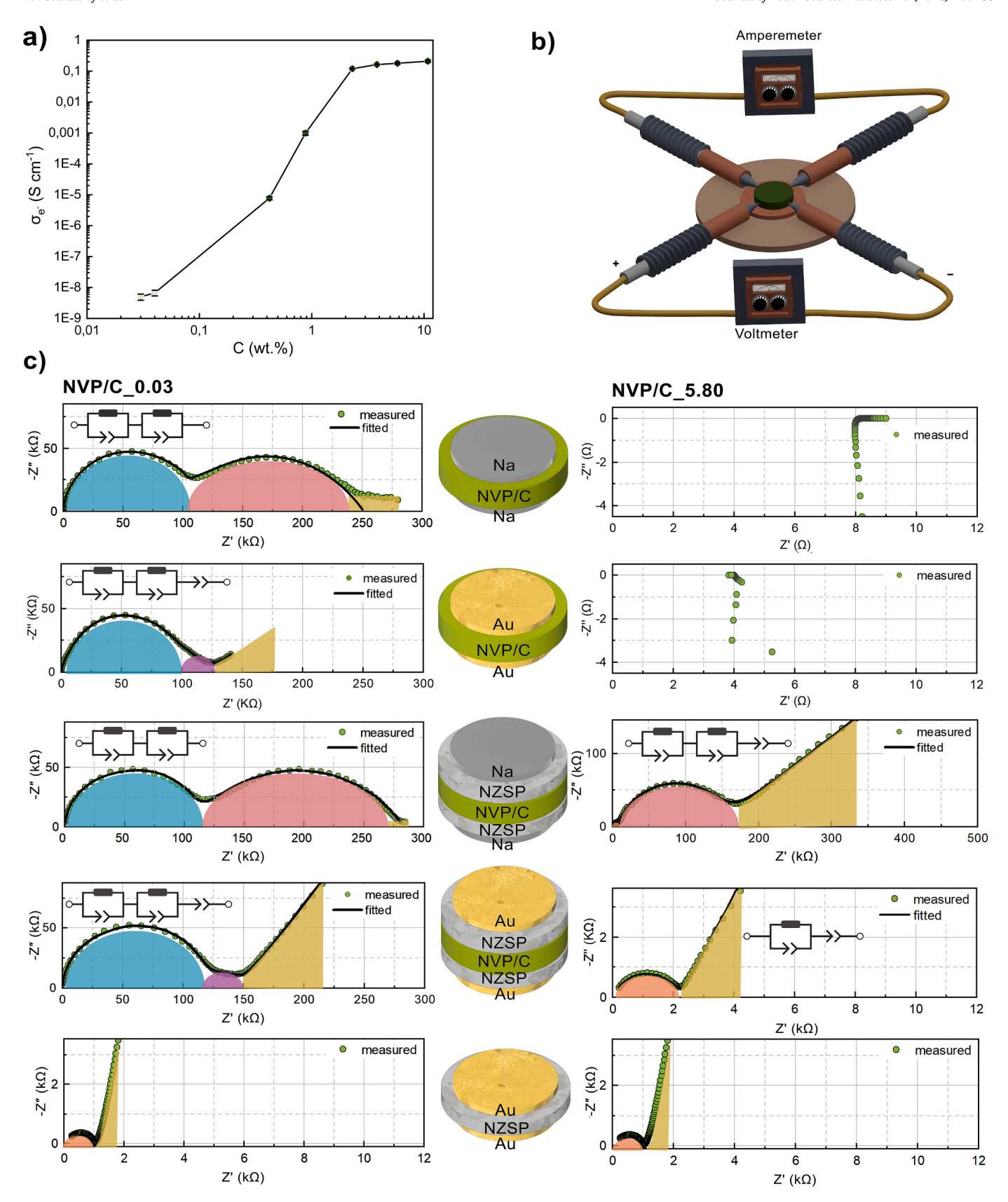


Fig. 4. a) Electronic conductivity of NVP/C samples. The open circles represent data derived from chronoamperometry and closed circles represent four-point measurements. b) Electrode setup for four-point measurements, c) impedance spectra of different electrodes on different configurations using NVP/C_0.03 and NVP/C_5.8 to better understand the ionic conductivity. The color code of semicircles represents grain boundary resistance of NVP (blue), constriction effect of Na metal (red), charge transfer resistance at the NVP/C and electrode interface (violet), the ionic resistance of NZSP (orange), diffusion-controlled Na⁺ ions in the electrode (yellow) to better visualize the processes. (For interpretation of the references to color in this figure legend, the reader is referred to the Web version of this article.)

3.4.3.1. Configuration [electrode|NVP/C|electrode]. Although the impedance responses from different electrodes are not similar (Fig. 4c, left), the first semicircle at high frequencies corresponds to the contribution of ionic resistance and the geometrical capacitance (CPE) of NVP/C (blue semicircle). It does not depend on the electrode material. NVP/C_0.03 with Na electrodes shows two semicircles and the second semicircle corresponds to the electrical resistance and the geometrical capacitance (CPE) of the NVP/C interfaced with Na metal (red semicircle). Other work attributed the second semicircle at mid-frequency to the dynamic constriction effect of the Na electrode [39]. The tail at low frequencies belongs to the Na metal and is difficult to detect because of the dominance of electric current (shunt) over the interfacial capacitance (yellow trapezoid) [47].

NVP/C_5.80, however, shows an impedance response with resistor and inductor in parallel and at low frequencies $Z^{\prime\prime}=0$, providing the resistance of the conducting carbon (Fig. 4c, right). Although amorphous carbon is relatively disordered according to the I_D/I_G ratio of 0.92, it is sufficient for the electrons to find a conductive route with minimal resistance.

When NVP/C_0.03 is contacted with Au electrodes, it shows one big semicircle at high frequencies, reflecting the ionic resistance of NVP, and a small semicircle at medium frequency that can be attributed to the charge transfer/interfacial resistance. Furthermore, at lower frequencies, the impedance is limited by the diffusion of Na $^+$ ions in the Au electrode. Instead, NVP/C_5.8 shows a straight inductive line with a similar response to that of the Na electrodes.

3.4.3.2. Configuration [electrode]NZSP|NVP/C|NZSP|electrode]. NVP/C_0.03 between two electrolyte layers and contacted with Na electrodes exhibits a similar response as without the electrolyte layers. The contribution of NZSP is negligible as it appears at higher frequencies with a total resistance of $\sim 1~k\Omega$ (1.2 mS cm $^{-1}$), as shown in Fig. 4c, bottom.

When NVP/C_5.80 is contacted with Na electrodes in this configuration, the electrolyte response can be seen at high frequencies, followed by the ionic resistance and capacitance response of NVP at medium frequencies. The response at medium frequencies can be attributed to the dynamic and geometrical constriction of the Na electrode [39]. At low frequencies, the presence of a Warburg impedance element appears. This could also be interpreted as a charge-transfer resistance and a double-layer capacitance. Nevertheless, it shows that the diffusion of Na $^+$ ions in Na metal is controlled by mass transportation [47,48]. The chronoamperometry of tri-layer NVP/C_0.03 and NVP/C_5.80 samples with a sodium electrode (shown in Fig. S3) confirms the ionic resistance of the samples and the ionic conductivity of NVP/C_5.80 (5.8 \pm 0.4

 $10^{-6}~S~cm^{-1}$) is found to be more than thrice that of NVP/C_0.03 (1.8 \pm 0.2 \times $10^{-6}~S~cm^{-1}$). The order of magnitude of ionic conductivity of NVP/C samples, however, remained constant, similar to previously reported values [12,25].

In addition, with Au electrodes, the NVP/C_0.03 sandwiched between NZSP electrolyte layers shows similar behavior to NVP/C_0.03 without NZSP. However, it exhibited an extended electrode response at low frequencies. In contrast, it is interesting to see the NZSP response in the impedance spectrum of NVP/C_5.80 (Fig. 4c, right). We postulate that the electronic conductivity of NVP/C_5.80 is much higher than the response from the electrolyte. Therefore, the impedance signal is not within the instrumental frequency range, only the electrolyte resistance parallel to the capacitance response is visible.

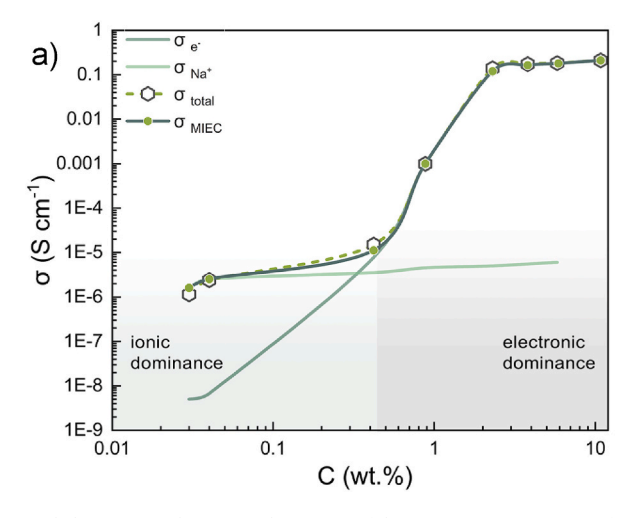
3.4.4. Mixed electronic and ionic conductivity

The total conductivities (Table 3) along with the conductivity values obtained from electronic and ionic measurements (Fig. 4) from different samples are shown in Fig. 5a. It is obvious from the graph that there are two regions with ionic conductivity dominance and electronic conductivity dominance. The MIEC line is obtained by adding electronic (Fig. 4a) and ionic conductivity (Fig. 4c) using equation (3):

$$\sigma_{MIEC} = \sigma_{e^-} + \sigma_{Na^+}$$
 Eq. (3)

The obtained mixed conductivity values are in very good agreement with the measured total conductivity values (σ_{total}) obtained from NVP/C samples with Au as ion-blocking electrodes (Fig. 3). The ionic conductivity of the NVP/C samples remains nearly constant within the same order of magnitude. The higher electrical conductivity reported previously [23,24,26] is proven to be a measurement of the carbon at grain boundaries and in the bulk of the samples resulting from electronic conductivity (see Table 1). Hence, this determination of the ionic and electronic dominance region of NVP/C proves that most of the reported conductivity data of NVP/C are strongly influenced by the presence of the carbon.

Fig. 5b compares of the total conductivity of the composites with amorphous carbon formed in-situ and particulate mixtures densified by cold sintering [22]. It is interesting to note that the three materials combinations follow a similar trend, but the percolation threshold at which the electronic conduction become dominant, is observed at 1 vol %, 2.4 vol%, and 3.8 vol% for the amorphous carbon, nano-particle-sized carbon powder and carbon fibers, respectively. The obtained maximum conductivity at high carbon contents follows the same sequence, i.e. 0.18 S cm⁻¹, 0.027 S cm⁻¹, and 0.005 S cm⁻¹, respectively. The decrease in conductivity is influenced, on the one hand,



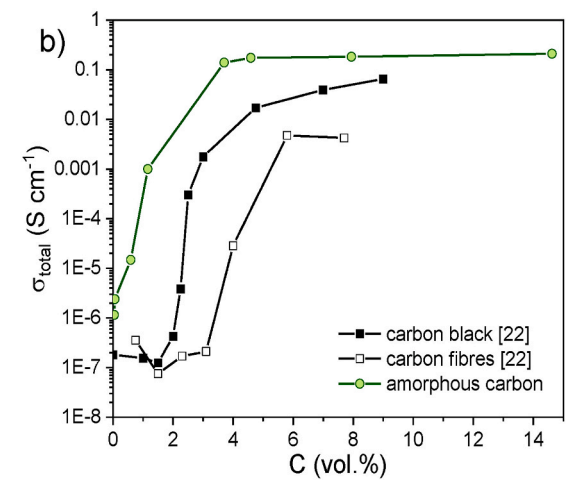


Fig. 5. a) Mixed electronic and ionic conductivities of the NVP/C composites as a function of carbon content, b) comparison of the determined σ_{total} values with those obtained with composites made by cold sintering and additions of carbon particles [22].

by the processing temperature (375 $^{\circ}\text{C}$ during cold sintering and 800 $^{\circ}\text{C}$ during SPS) and, on the other hand, by the addition of NaOH as a sintering aid during cold sintering, which could interfere with the conduction along the grain boundaries.

4. Conclusion

NVP/C powders with varying carbon content were prepared and subsequently densified with FAST/SPS. Two different configurations and two different electrode materials were used to identify the ionic and electronic conductivities of the individual samples. The NVP/C with carbon contents > 0.1 wt% showed a higher degree of densification due to the ability of surface carbon to diffuse and densify the sample during sintering. The amount of hexagonal structure units increases with increasing carbon percentage. The total conductivity of the NVP/C measured with ion-blocking electrodes proved to contain both ionic and electronic conductivity, which highly depends on the amount of carbon in the sample. Changing the electrodes from Au to Na using different configurations allowed the ionic dominance and electronic dominance regions of NVP/C to be determined. This study confirms that samples with either high ionic conductivity ($\sigma_{ionic} \gg \sigma_{electronic}$) or high electronic conductivity ($\sigma_{electronic} \gg \sigma_{ionic})$ require different measurement conditions in terms of electrodes and sample configurations (ion-blocking vs. non-ion-blocking). The ionic conductivity of NVP/C remains unchanged, as it is a material property that cannot be changed by a coating or by increasing the carbon content. However, further investigations are necessary to determine the electrochemical performances of these composite materials and to elucidate the influence of the carbon content on the charging and discharging processes.

CRediT authorship contribution statement

Pradhyun Veerapanaicker Soundaraj: Writing – review & editing, Writing – original draft, Visualization, Investigation. Enkhtsetseg Dashjav: Writing – review & editing, Validation, Supervision, Investigation. Daniel Grüner: Writing – review & editing, Investigation. Stephan Prünte: Writing – review & editing, Investigation. Christian Dellen: Writing – review & editing, Investigation. Frank Tietz: Writing – review & editing, Supervision, Project administration, Funding acquisition, Conceptualization.

Declaration of competing interest

The authors declare the following financial interests/personal relationships which may be considered as potential competing interests: Frank Tietz reports financial support was provided by German Federal Ministry of Education and Research. If there are other authors, they declare that they have no known competing financial interests or personal relationships that could have appeared to influence the work reported in this paper.

Data availability

Data will be made available on request.

Acknowledgements

The authors thank Dr. M. Ihrig for initial SPS instructions and M.-T. Gerhards for the preparation of NZSP powders. Financial support from the German Federal Ministry of Education and Research (BMBF) within the projects "HeNa" (support code 13XP0390B) and "NASS" (support code 13XP0490B) is gratefully acknowledged. The authors take responsibility for the content of this publication.

Appendix A. Supplementary data

Supplementary data to this article can be found online at $\frac{\text{https:}}{\text{doi.}}$ org/10.1016/j.powera.2024.100144.

References

- [1] X. Zhang, X. Rui, D. Chen, H. Tan, D. Yang, S. Huang, Y. Yu, Na₃V₂(PO₄)₃: an advanced cathode for sodium-ion batteries, Nanoscale 11 (2019) 2556–2576, https://doi.org/10.1039/c8nr09391a.
- [2] T.E. Graedel, E.M. Harper, N.T. Nassar, P. Nussa, B.K. Reck, Criticality of metals and metalloids, Proc. Natl. Acad. Sci. USA 112 (2015) 4257–4262. https://www. pnas.org/doi/10.1073/pnas.1500415112.
- [3] P. Palandrani, Four Companies Leading the Rise of Lithium & Battery Technology, 2000. https://globalxetfs.co.jp/en/research/four-companies-leading-the-rise-of-li thium-battery-technology/index.html. visited 25, 09, 2023.
- [4] C. Delmas, R. Olazcuaga, F. Cherkaoui, R. Brochu, G. Le Flem, Sur une nouvelle famille de phosphates de formule Na₃M₂(PO₄)₃ (M= Ti, V, Cr, Fe), Comptes Rendus Hebd. Des Séances l'Académie, Des Sci. Série C, Sci. Chim. 287 (1978) 169–171.
- [5] Z. Jian, L. Zhao, H. Pan, Y.S. Hu, H. Li, W. Chen, L. Chen, Carbon coated Na₃V₂(PO₄)₃ as novel electrode material for sodium ion batteries, Electrochem. Commun. 14 (2012) 86–89, https://doi.org/10.1016/j.elecom.2011.11.009.
- [6] M.E. Brownfield, E.E. Foord, S.J. Sutley, T. Botinelly, Kosnarite, KZr₂(PO₄)₃, a new mineral from mount Mica and black mountain, Oxford county, Maine, Am. Mineral. 78 (1993) 653–656.
- [7] Q. Ma, F. Tietz, Solid-state electrolyte materials for sodium batteries: towards practical applications, Chemelectrochem 7 (2020) 2693–2713, https://doi.org/ 10.1002/celc.202000164.
- [8] Y. Ruan, F. Guo, J. Liu, S. Song, N. Jiang, B. Cheng, Optimization of Na₃Zr2Si₂PO₁₂ ceramic electrolyte and interface for high performance solid-state sodium battery, Ceram. Int. 45 (2019) 1770–1776, https://doi.org/10.1016/j.ceramint.2018.10.062.
- [9] S.-C. Yin, H. Grondey, P. Strobel, M. Anne, L.F. Nazar, Electrochemical property: structure relationships in monoclinic Li_{3-y}V₂(PO₄)₃, J. Am. Chem. Soc. 125 (2003) 10402–10411, https://doi.org/10.1021/ja034565h.
- [10] S. Chen, C. Wu, L. Shen, C. Zhu, Y. Huang, K. Xi, J. Maier, Y. Yu, Challenges and perspectives for NASICON-type electrode materials for advanced, Sodium-Ion Batteries 29 (2017) 1700431, https://doi.org/10.1002/adma.201700431.
- [11] S.-Y. Chung, J.T. Bloking, Y.-M. Chiang, Electronically conductive phosphoolivines as lithium storage electrodes, Nat. Mater. 1 (2002) 123–128, https://doi. org/10.1038/nmat/32.
- [12] T. Lan, Q. Ma, C.-L. Tsai, F. Tietz, O. Guillon, Ionic conductivity of Na₃V₂(PO₄)₃ as a function of electrochemical potential and its impact on battery performance, Batteries Supercaps 4 (2021) 479–484, https://doi.org/10.1002/batt.202000229.
- [13] H. Wang, D. Jiang, Y. Zhang, G. Li, X. Lan, H. Zhong, Z. Zhang, Y. Jiang, Self-combustion synthesis of Na₃V₂(PO₄)₃ nanoparticles coated with carbon shell as cathode materials for sodium-ion batteries, Electrochim. Acta 155 (2015) 23–28, https://doi.org/10.1016/j.electacta.2014.12.160.
- [14] L. Li, S. Peng, J.K.Y. Lee, D. Ji, M. Srinivasan, S. Ramakrishna, Electrospun hollow nanofibers for advanced secondary batteries, Nano Energy 39 (2017) 111–139, https://doi.org/10.1016/j.nanoen.2017.06.050.
- [15] J. Liu, K. Tang, K. Song, P.A. Van Aken, Y. Yu, J. Maier, Electrospun Na₃V₂(PO₄)₃/ C nanofibers as stable cathode materials for sodium-ion batteries, Nanoscale 6 (2014) 5081–5086, https://doi.org/10.1039/c3nr05329f.
- [16] S. Tao, P. Cui, W. Huang, Z. Yu, X. Wang, S. Wei, D. Liu, L. Song, W. Chu, Sol-gel design strategy for embedded Na₃V₂(PO₄)₃ particles into carbon matrices for high-performance sodium-ion batteries, Carbon 96 (2016) 1028–1033, https://doi.org/10.1016/j.carbon.2015.10.054.
- [17] Z. Chu, C. Yue, Core-shell structured Na₃V₂(PO₄)₃/C nanocrystals embedded in multi-walled carbon nanotubes: a high-performance cathode for sodium-ion batteries, Solid State Ionics 287 (2016) 36–41, https://doi.org/10.1016/j. ssi 2015 07 024
- [18] H. Li, X. Yu, Y. Bai, F. Wu, C. Wu, L.Y. Liu, X.Q. Yang, Effects of Mg doping on the remarkably enhanced electrochemical performance of Na₃V₂(PO₄)₃ cathode materials for sodium ion batteries, J. Mater. Chem. A 3 (2015) 9578–9586, https:// doi.org/10.1039/c5ta00277i.
- [19] A. Inoishi, Y. Yoshioka, L. Zhao, A. Kitajou, S. Okada, Improvement in the energy density of Na₃V₂(PO₄)₃ by Mg substitution, Chemelectrochem 4 (2017) 2755–2759, https://doi.org/10.1002/celc.201700540.
- [20] R. Klee, P. Lavela, M.J. Aragón, R. Alcántara, J.L. Tirado, Enhanced high-rate performance of manganese substituted Na₃V₂(PO₄)₃/C as cathode for sodium-ion batteries, J. Power Sources 313 (2016) 73–80, https://doi.org/10.1016/j. jpowsour.2016.02.066.
- [21] M.J. Aragón, P. Lavela, G.F. Ortiz, J.L. Tirado, Effect of iron substitution in the electrochemical performance of Na₃V₂(PO₄)₃ as cathode for Na-ion batteries, J. Electrochem. Soc. 162 (2015) A3077–A3083, https://doi.org/10.1149/ 2.0151502jes.
- [22] Z.M. Grady, Z. Fan, J. Fanghanel, C.A. Randall, Conductivity of cold sintered diphasic composites containing a ceramic active material and a solid-state electrolyte or carbon for all solid-state batteries, J. Mater. Chem. A 12 (2024) 4492–4512, https://doi.org/10.1039/d3ta07067k.
- [23] A. Chekannikov, R. Kapaev, S. Novikova, N. Tabachkova, T. Kulova, A. Skundin, A. Yaroslavtsev, Na₃V₂(PO₄)₃/C/Ag nanocomposite materials for Na-ion batteries

- obtained by the modified Pechini method, J. Solid State Electrochem. 21 (2017) 1615–1624, https://doi.org/10.1007/s10008-017-3524-4.
- [24] H. Wang, G. Hasegawa, Y. Akiyama, T. Yamamoto, A. Inoishi, H. Akamatsu, M. Inada, T. Ishihara, K. Hayashi, A highly conductive Na₃V₂(PO₄)₃ ceramic sheet prepared by tape-casting method, Electrochim, Acta 305 (2019) 197–203, https://doi.org/10.1016/j.electacta.2019.03.057.
- [25] H. Ma, B. Zhao, J. Bai, K. Li, Z. Fang, P. Wang, W. Li, X. Zhu, Y. Sun, Improved electrochemical performance of Na₃V_{2-x}Zr_x(PO₄)₃/C through electronic and ionic conductivities regulation, J. Electrochem. Soc. 167 (2020) 070548, https://doi.org/10.1149/1945-7111/ab812b.
- [26] Y. Chen, Y. Xu, X. Sun, B. Zhang, S. He, C. Wang, F-doping and V-defect synergetic effects on Na₃V₂(PO₄)₃/C composite: a promising cathode with high ionic conductivity for sodium ion batteries, J. Power Sources 397 (2018) 307–317, https://doi.org/10.1016/j.jpowsour.2018.07.006.
- [27] Q. Ma, C.L. Tsai, X.K. Wei, M. Heggen, F. Tietz, J.T.S. Irvine, Room temperature demonstration of a sodium superionic conductor with grain conductivity in excess of 0.01 S cm⁻¹ and its primary applications in symmetric battery cells, J. Mater. Chem. A 7 (2019) 7766–7776, https://doi.org/10.1039/c9ta00048h.
- [28] F. Lalère, J.B. Leriche, M. Courty, S. Boulineau, V. Viallet, C. Masquelier, V. Seznec, An all-solid state NASICON sodium battery operating at 200 °C, J. Power Sources 247 (2014) 975–980, https://doi.org/10.1016/j.jpowsour.2013.09.051.
- [29] Y. Noguchi, E. Kobayashi, L.S. Plashnitsa, S. Okada, J.I. Yamaki, Fabrication and performances of all solid-state symmetric sodium battery based on NASICONrelated compounds, Electrochim. Acta 101 (2013) 59–65, https://doi.org/ 10.1016/j.electacta.2012.11.038.
- [30] D. Kutsuzawa, T. Kobayashi, S. Komiya, Flux-assisted low-temperature fabrication of highly durable all-oxide solid-state sodium-ion batteries, ACS Appl. Energy Mater. 5 (2022) 4025–4028, https://doi.org/10.1021/acsaem.2c00365.
- [31] M.J. Wang, J.B. Wolfenstine, J. Sakamoto, Mixed electronic and ionic conduction properties of lithium lanthanum titanate, Adv. Funct. Mater. 30 (2020) 1909140, https://doi.org/10.1002/adfm.201909140.
- [32] L.J. van der Pauw, A Method of measuring specific resistivity and hall effect of discs of arbitrary shape, Philips Res. Rep. 13 (1958) 1–9.
- [33] M. Iwaki, Estimation of the atomic density of amorphous carbon using ion implantation, SIMS and RBS, Surf. Coating. Technol. 158–159 (2002) 377–381, https://doi.org/10.1016/S0257-8972(02)00247-5.
- [34] O. Guillon, J. Gonzalez-Julian, B. Dargatz, T. Kessel, G. Schierning, J. Räthel, M. Herrmann, Field-assisted sintering technology/spark plasma sintering: mechanisms, materials, and technology developments, Adv. Eng. Mater. 16 (2014) 830–849, https://doi.org/10.1002/adem.201300409.
- [35] R.K. Bordia, S.J.L. Kang, E.A. Olevsky, Current understanding and future research directions at the onset of the next century of sintering science and technology, J. Am. Ceram. Soc. 100 (2017) 2314–2352, https://doi.org/10.1111/jace.14919.
- [36] A.C. Ferrari, J. Robertson, Interpretation of Raman spectra of disordered and amorphous carbon, Phys. Rev. B Condens. Matter 61 (2000) 14095–14107, https://doi.org/10.1103/PhysRevB.61.14095.

- [37] K. Müllen, C. Castiglioni, G. Zerbi, Common force field for graphite and polycyclic aromatic hydrocarbons, Phys. Rev. B Condens. Matter 60 (1999) 12710–12725, https://doi.org/10.1103/PhysRevB.60.12710.
- [38] Q. Ni, Y. Bai, Y. Li, L. Ling, L. Li, G. Chen, Z. Wang, H. Ren, F. Wu, C. Wu, 3D electronic channels wrapped large-sized Na₃V₂(PO₄)₃ as flexible electrode for sodium-ion batteries, Small 14 (2018) 1702864, https://doi.org/10.1002/smll.201702864
- [39] J.K. Eckhardt, P.J. Klar, J. Janek, C. Heiliger, Interplay of dynamic constriction and interface morphology between reversible metal anode and solid electrolyte in solid state batteries, ACS Appl. Mater. Interfaces 14 (2022) 35545–35554, https://doi. org/10.1021/acsami.2c07077.
- [40] F.S. Oliveira, R.B. Cipriano, F.T. da Silva, E.C. Romão, C.A.M. dos Santos, Simple analytical method for determining electrical resistivity and sheet resistance using the van der Pauw procedure, Sci. Rep. 10 (2020) 1–8, https://doi.org/10.1038/ s41598-020-72097-1.
- [41] A. Kežionis, P. Butvilas, T. Šalkus, S. Kazlauskas, D. Petrulionis, T. Žukauskas, E. Kazakevičius, A.F. Orliukas, Four-electrode impedance spectrometer for investigation of solid ion conductors, Rev. Sci. Instrum. 84 (2013) 013902, https:// doi.org/10.1063/1.4774391.
- [42] Y. Zhao, X. Cao, G. Fang, Y. Wang, H. Yang, S. Liang, A. Pan, G. Cao, Hierarchically carbon-coated Na₃V₂(PO₄)₃ nanoflakes for high-rate capability and ultralong cyclelife sodium ion batteries, Chem. Eng. J. 339 (2018) 162–169, https://doi.org/10.1016/j.cej.2018.01.088.
- [43] G. Li, D. Jiang, H. Wang, X. Lan, H. Zhong, Y. Jiang, Glucose-assisted synthesis of Na₃V₂(PO₄)₃/C composite as an electrode material for high-performance sodiumion batteries, J. Power Sources 265 (2014) 325–334, https://doi.org/10.1016/j. jpowsour.2014.04.054.
- [44] Y. Jiang, Z. Yang, W. Li, L. Zeng, F. Pan, M. Wang, X. Wei, G. Hu, L. Gu, Y. Yu, Nanoconfined carbon-coated Na₃V₂(PO₄)₃ particles in mesoporous carbon enabling ultralong cycle life for sodium-ion batteries, Adv. Energy Mater. 5 (2015) 1–8, https://doi.org/10.1002/aenm.201402104.
- [45] W. Shen, C. Wang, H. Liu, W. Yang, Towards highly stable storage of sodium ions: a porous Na₃V₂(PO₄)₃/C cathode material for sodium-ion batteries, Chem. Eur J. 19 (2013) 14712–14718, https://doi.org/10.1002/chem.201300005.
- [46] Y. Jiang, X. Zhou, D. Li, X. Cheng, F. Liu, Y. Yu, Highly reversible Na storage in Na₃V₂(PO₄)₃ by optimizing nanostructure and rational surface engineering, Adv. Energy Mater. 8 (2018) 1–7, https://doi.org/10.1002/aenm.201800068.
- [47] R.A. Huggins, Simple method to determine electronic conductivity and ionic components of the conductors in mixed a review, Ionics 8 (2002) 300–313, https://doi.org/10.1007/BF02376083.
- [48] Y. Iriyama, T. Kako, C. Yada, T. Abe, Z. Ogumi, Charge transfer reaction at the lithium phosphorus oxynitride glass electrolyte/lithium cobalt oxide thin film interface, Solid State Ionics 176 (2005) 2371–2376, https://doi.org/10.1016/j. ssi 2005 02 025